Draft version February 8, 2019
Typeset using LaTeX **manuscript** style in AASTeX62

Minerva-Australis I: Design, Commissioning, & First Photometric Results

Brett Addison,[1] Duncan J. Wright,[1] Robert A. Wittenmyer,[1] Jonathan Horner,[1] Matthew W. Mengel,[1] Daniel Johns,[2] Connor Marti,[3] Belinda Nicholson,[1] Jack Okumura,[1] Brendan Bowler,[4] Ian Crossfield,[5] Stephen R. Kane,[6] John Kielkopf,[7] Peter Plavchan,[8] C.G. Tinney,[9] and Hui Zhang[10]

[1] *University of Southern Queensland, Centre for Astrophysics, West Street, Toowoomba, QLD 4350 Australia*

[2] *Department of Physical Sciences, Kutztown University, Kutztown, PA 19530, USA*

[3] *Department of Astronomy, Williams College, 33 Lab Campus Drive, Williamstown, MA 01267 USA*

[4] *Department of Astronomy, The University of Texas at Austin, TX 78712, USA*

[5] *Department of Physics, Massachusetts Institute of Technology, Cambridge, MA, USA*

[6] *Department of Earth Sciences, University of California, Riverside, CA 92521, USA*

[7] *Department of Physics and Astronomy, University of Louisville, Louisville, KY 40292, USA*

[8] *Department of Physics & Astronomy, George Mason University, 4400 University Drive MS 3F3, Fairfax, VA 22030, USA*

[9] *Exoplanetary Science at UNSW, School of Physics, UNSW Sydney, NSW 2052, Australia*

[10] *School of Astronomy and Space Science, Key Laboratory of Modern Astronomy and Astrophysics in Ministry of Education, Nanjing University, Nanjing 210046, Jiangsu, China*

(Accepted January 30, 2019)

Submitted to Publications of the Astronomical Society of the Pacific

ABSTRACT

The Minerva-Australis telescope array is a facility dedicated to the follow-up, confirmation, characterisation, and mass measurement of bright transiting planets discovered by the Transiting Exoplanet Survey Satellite (*TESS*) – a category in which it is almost unique in the southern hemisphere. It is located at the University of Southern Queensland's Mount Kent Observatory near Toowoomba, Australia. Its flexible design enables multiple 0.7 m robotic telescopes to be used both in combination, and independently,

for high-resolution spectroscopy and precision photometry of *TESS* transit planet candidates. MINERVA-Australis also enables complementary studies of exoplanet spin-orbit alignments via Doppler observations of the Rossiter-McLaughlin effect, radial velocity searches for non-transiting planets, planet searches using transit timing variations, and ephemeris refinement for *TESS* planets. In this first paper, we describe the design, photometric instrumentation, software, and science goals of MINERVA-Australis, and note key differences from its Northern hemisphere counterpart – the MINERVA array. We use recent transit observations of four planets–WASP-2b, WASP-44b, WASP-45b, and HD 189733b to demonstrate the photometric capabilities of MINERVA-Australis.

1. INTRODUCTION

There has long been interest in the discovery of planets around other stars. Early attempts to find such worlds, however, got off to a slow and rocky start with several exoplanetary detection claims being either later retracted, or never confirmed – such as the proposed planets orbiting 70 Ophiuchi (Jacob 1855), Barnard's Star, (van de Kamp 1963; Gatewood 1995), and the pulsar PSR B1829-10 (Bailes et al. 1991; Lyne & Bailes 1992)). It wasn't until the announcement of the first confirmed exoplanet orbiting a Sun-like star in 1995 (51 Pegasi b, Mayor & Queloz 1995) that truly kicked off the "Exoplanet Era".

In the years immediately following that discovery, the number of confirmed exoplanets grew slowly. As we have become ever more adept at finding new planets, however, the number known has grown exponentially, especially over the last decade. This is due, in large part, to the extremely successful *Kepler* mission launched by NASA in 2009 (Koch et al. 2010) to search for planets via their transits. The spacecraft's four year primary mission, together with its more recent K2 program extension (Howell et al. 2014) have confirmed the existence of over 2500 planets[1], including many that resemble nothing found in the Solar System.

[1] See https://exoplanetarchive.ipac.caltech.edu/ for the latest tally.

This incredible diversity includes the so-called 'hot Jupiters' and 'hot Neptunes' (e.g., Mayor & Queloz 1995; Charbonneau et al. 2000; Gillon et al. 2007; Bakos et al. 2010; Bayliss et al. 2013), planets moving on extremely eccentric orbits (e.g., Jones et al. 2006; Wittenmyer et al. 2017), planets with densities greater than iron and even osmium (e.g., Deleuil et al. 2008; Dumusque et al. 2014; Johns et al. 2018), or comparable to styrofoam (e.g., Faedi et al. 2011; Welsh et al. 2015; Pepper et al. 2017). Perhaps most surprisingly, *Kepler* revealed that planets between the size of Earth and Neptune ('super-Earths') are incredibly common, despite the fact that no analogue exists in the Solar System (e.g., Charbonneau et al. 2009; Barragán et al. 2018).

The primary goals of *Kepler* were to perform a detailed exoplanet census and to measure the frequency distribution function for planets around other stars. This was accomplished by continually monitoring ∼150,000 stars in the northern constellation of Cygnus for transits (Koch et al. 2010) for a period in excess of four years. Chief among *Kepler*'s results is the revelation that planets are ubiquitous, and that the majority of stars host small planets, with mini-Neptunes and super-Earths being the most common of those found on orbits of $\leq$ 200 days (Fressin et al. 2013). *Kepler* also revealed that Earth-sized planets ($0.5 \leq R_P \leq 1.4 R_\oplus$) are particularly common around cool stars ($T_{\rm eff} \leq 4000\,{\rm K}$), with an occurrence rate of just over 50 percent (Dressing & Charbonneau 2013). Indeed, based on *Kepler* data, Dressing & Charbonneau (2013) estimated the occurrence rate of Earth-size planets in the habitable zone as $0.15^{+0.13}_{-0.06}$ planets per cool star. This suggest that the nearest transiting Earth-size planet in the habitable zone could be located within 21 pc of Earth.

Despite the stunning success of the *Kepler* mission, little is known about the compositions, masses, and densities of the majority of the *Kepler* planets. The reason for this is that the majority of the planet hosting stars identified by *Kepler* are either too faint for further follow-up investigations using existing facilities, or would require an inordinate investment of time on large telescopes. Because of the significant resources that are required to convert the large number of *Kepler* candidates into

confirmed planets and measure their masses, only about 50% of *Kepler*'s candidate planets have been confirmed and of the confirmed planets, only $\sim 10\%$ have mass measurements[2].

On 2018 April 18, NASA launched its next generation exoplanet finder, the Transiting Exoplanet Survey Satellite (*TESS*, Ricker et al. 2015). Unlike *Kepler*, which observed a single small region on the sky, *TESS* expands the search for planets to nearly the entire sky. *TESS* consists of four wide-angle cameras that each have a field of view of $24^\circ \times 24^\circ$, yielding a total field of view for *TESS* of $96^\circ \times 24^\circ$. The spacecraft is oriented such that one of the cameras is centered on one of the ecliptic poles whilst the others are pointed progressively closer to the ecliptic. *TESS* will monitor each 24° wide strip on the celestial sphere for a period of 27 days before moving on to an adjacent strip of the sky. As such, the majority of stars will be observed for 27 days, while those closer to the ecliptic poles will be observed for longer. As a result of this strategy, stars within $\sim 12^\circ$ of the ecliptic poles will be observed for a year. *TESS* will observe the southern ecliptic hemisphere in its first year of operation before moving on to the northern ecliptic hemisphere in the second year of its mission.

Through the course of its initial two-year mission, *TESS* will survey approximately 200,000 of the brightest stars in the sky with a cadence of two minutes. Planets discovered around these bright stars will be suitable for ground based follow-up observations to both confirm their existence, and to facilitate their characterisation (e.g. Huang et al. 2018; Gandolfi et al. 2018). Data will also be returned on an additional 20 million stars from "full frame images", taken with a cadence of 30 minutes. As a result, there will be no shortage of planet candidates coming from *TESS* that will need follow-up observations. Additionally, stars observed by *TESS* will be, on average, a hundred times brighter than those observed by *Kepler*, and it is expected that *TESS* will deliver a yield of thousands of new planets orbiting bright stars.

With the expected flood of planet candidates being found by *TESS* orbiting bright stars, dedicated facilities are urgently needed to confirm the candidates and characterise them. The radial velocity technique is the primary method to deliver the critical planetary parameters, such as a planet's mass

[2] Determined using the NASA Exoplanet Archive (https://exoplanetarchive.ipac.caltech.edu/). There are 2347 confirmed *Kepler* planets and 244 of them have mass measurements listed in the table.

and orbital eccentricity, that are required to properly characterise the planetary system. Most of the existing facilities capable of carrying out the required high precision radial velocity measurements, however, are subject to intense competition and scheduling constraints (particularly on shared large telescopes). Traditionally, radial velocity programs are allocated blocks of time (a couple of weeks to a month) on large telescopes during bright nights (though some such as the Hobby-Eberly Telescope and WIYN are working to facilitate queue and cadence observations).

With the expected large number of planet candidates to be delivered by *TESS*, the most exciting of which will be low-mass planets with orbital periods exceeding one month (in particular those planets orbiting within the habitable zone around M-dwarf stars), this strategy simply will not work. This is the primary cause of the significant bottlenecks experienced during the follow-up work carried out on *Kepler* candidates (Fleming et al. 2015).

Similarly with *TESS*, we will be in a situation where we have too many planets, and too few telescopes to confirm them.

To address this bottleneck issue with *TESS* follow-up, we are commissioning the MINERVA-Australis facility at the University of Southern Queensland's Mount Kent Observatory (MKO). MINERVA-Australis builds on the template and groundwork of a similar facility in the northern hemisphere called MINERVA (MINiature Radial Velocity Array) located at Mt. Hopkins, in the Arizona desert (Swift et al. 2015). Whereas the primary goal of the Northern MINERVA observatory is to search for small-mass planets orbiting nearby bright stars through high-cadence radial velocity observations, MINERVA-Australis will be primarily focused on supporting the follow-up work of NASA's *TESS* mission.

The MINERVA-Australis collaboration consists of the University of Southern Queensland as the primary investigator along with the University of Texas at Austin, Massachusetts Institute of Technology, University of California at Riverside, University of Louisville, George Mason University, the University of New South Wales, University of Florida, and Nanjing University as co-investigators and major funding partners in this project. It is also a participating member of the TESS Follow-up Ob-

serving Program (TFOP[3]) Working Group (WG). The primary goal of TFOP WG is to coordinate the follow-up observations of TESS planet candidates to measure masses for 50 transiting planets smaller than 4 Earth radii. Additionally, TFOP WG is fostering communication and coordination within its network of participants and community at large to optimise the follow-up work of TESS planet candidates and minimise wasteful duplication of observations and analysis. MINERVA-Australis is primarily involved in two of the TFOP Sub Groups (SG), SG2 for reconnaissance spectroscopy and SG4 for precision radial velocity work.

Secondary science objectives for the MINERVA-Australis project include the measurement of the spin-orbit alignment of planetary systems through radial velocity and Doppler tomography observations of the Rossiter-McLaughlin effect (Rossiter 1924; McLaughlin 1924; Queloz et al. 2000; Johnson et al. 2014; Addison et al. 2018). Spin-orbit alignments can provide key insights into the formation and migration histories of exoplanets (e.g., see, Lin et al. 1996; Bodenheimer et al. 2000; Ford & Rasio 2008; Naoz et al. 2011; Wu & Lithwick 2011), in particular hot (Crida & Batygin 2014; Winn & Fabrycky 2015) and warm Jupiters (Dong et al. 2014) and compact transiting multi-planet systems (Albrecht et al. 2013; Wang et al. 2018a). Additionally, Doppler tomography observations can also aid in the confirmation of transiting planet candidates orbiting rapidly rotating stars that are not amenable to precise radial velocity observations (Johnson et al. 2014). Another science goal is to carry out long term radial velocity monitoring of planetary systems found by *TESS*. Such observations could reveal the existence of non-transiting long-period planets that can provide constraints on the migration history of the inner transiting planet(s) (e.g. Otor et al. 2016; Christiansen et al. 2017; Almenara et al. 2018).

While spectroscopy and radial velocity observations are the primary focus of MINERVA-Australis, high-precision and high-cadence photometry is also an important component of this project.

Fluctuations observed in the out-of-transit photometry of a star can be used to disentangle the radial velocity variations that are produced by stellar activity, such as from starspots and from the

[3] https://tess.mit.edu/followup/

suppression of convective blueshift occurring in active regions on the stellar surface, from planetary signals (Boisse et al. 2011). This is particularly the case when photometry and radial velocity data are obtained simultaneously (Haywood et al. 2014), as can be done with MINERVA-Australis. Such data will provide a better understanding of the effects of stellar activity on radial velocity observations, enabling the detection of sub-Neptune mass planets and more accurate determinations of their masses.

Simultaneous photometry is also quite useful when carrying out Rossiter-McLaughlin effect observations. These observations are typically carried out several hundred orbital periods after the last published transit in the literature and the ephemerides have usually become out of date. Simultaneous photometry can be used to lock down the transit ingress, mid, and egress times needed for properly analysing Rossiter-McLaughlin data. Additionally, stellar activity can deform the Rossiter-McLaughlin signal that can cause significant variations in the measured spin-orbit angle (up to $\sim 42^{\circ}$) from transit to transit (Oshagh et al. 2018). Simultaneous photometry can provide information about the properties of the active regions on a stellar surface that will allow for better modeling of the Rossiter-McLaughlin signal (Oshagh et al. 2018).

While it is expected the majority of transiting planets detected by TESS will come from the pre-selected bright stars with a two minute cadence, undoubtedly some transit detections will come from the full frame images that are taken at a 30 minute cadence. These planets will require follow-up transit photometry to lock down the transit parameters that are not possible to obtain from the long cadence photometry. MINERVA-Australis will be utilised for this task as such planet candidates are found.

We will also be using photometry to search for transit timing variations (TTVs) through photometric transit observations that could reveal the presence of additional planets (Malavolta et al. 2017; Saad-Olivera et al. 2017) as well as transit observations to keep the transit ephemerides up-to-date for *TESS* planets.

Other ancillary science goals include observations of predicted Solar System occultation events. Such observations have yielded improved information on the size, shape, and albedo of small Solar System objects (Sicardy et al. 2011a,b; Ortiz et al. 2012) as well as led to the discovery of ring

systems around some of these minor bodies (Braga-Ribas et al. 2014a; Ortiz et al. 2017a). We are also planning on continuing the radial velocity follow-up of targets that were originally observed as part of the Anglo-Austrian Planet Search program (AAPS, e.g., Tinney et al. 2011; Wittenmyer et al. 2014) with the aim of extending the radial velocity data-set baseline to enable the detection of longer orbital period ($\geq 5\,\mathrm{yr}$) planets. By continuing the AAPS legacy survey, our goal is to expand the population of known Jupiter or Saturn analogues and determine the degree to which the Solar System is unusual or unique.

We have organised the manuscript as follows: Section 2 provides an overview of the Mount Kent Observatory and the reasons for selecting the site for MINERVA-Australis. Section 3 describes the MINERVA-Australis facilities and hardware, including the telescopes and enclosures, spectrograph, camera, and control building. In Section 4, we present the first science results from follow-up photometric transit observations of four transiting planets, including WASP-2b, WASP-44b, WASP-45b, and HD 189733b. Lastly, in Section 5 we summarise the MINERVA-Australis facility, goals, and future work.

2. MOUNT KENT OBSERVATORY

The MINERVA-Australis facility is being commissioned at the University of Southern Queensland's Mount Kent Observatory (MKO). MKO is located in the Darling Downs in Queensland, Australia, approximately 25 km south-southwest of Toowoomba and 120 km west-southwest of Brisbane. It is situated at an altitude of $\sim 680\,\mathrm{m}$ and a latitude and longitude of $27°47'53''\,\mathrm{S}$ and $151°51'20''\,\mathrm{E}$. The site already houses three telescopes of the Shared Skies project, operated jointly between the University of Louisville, Kentucky, and the University of Southern Queensland: the 0.1 m aperture wide field OMara robotic telescope, used for education, and two PlaneWave Instrument telescopes (a CDK20 and a CDK700) used for KELT[4] and *T*ESS precision exoplanet transit photometry followup. Figure 1 shows a Google Maps image of the MINERVA-Australis telescope sites, building location, and other facilities on the MKO.

[4] The Kilodegree Extremely Little Telescope survey (e.g. Pepper et al. 2007, 2012; Soutter et al. 2016)

Figure 1. Google Maps image of the Mount Kent Observatory showing the location of the MINERVA-Australis telescopes and building.

The Mount Kent site was selected based on good weather conditions almost year round with an average of ∼296 clear/mostly clear nights per year, reasonably good seeing conditions (estimated to be around 1.6″ from seeing measurements reported by the existing facilities at the site), and existing facilities and support. The weather data has been obtained from the Bureau of Meteorology website[5]

[5] http://www.bom.gov.au/

using the Oakey Aero weather station (a nearby weather station with 35 years of historic climate data) located about 44 km from Mount Kent. Conditions at the Oakey weather station should serve as a good proxy for the conditions observed at Mount Kent and give a good estimate of the number of usable nights. Therefore, we anticipate ~ 296[6] nights per year with observable weather conditions with at least an average of 6.7 usable hours and a median seeing of 1.6″.

3. FACILITIES

In this section, we give details of the MINERVA-Australis hardware, highlight the ways in which our new facility differs from the Northern MINERVA facility (Swift et al. 2015), and discuss the reasoning behind those choices.

3.1. *Telescopes and Enclosures*

MINERVA-Australis will comprise up to six independently operated 0.7 m PlaneWave CDK-700 altitude/azimuth mounted telescopes[7] (see Figure 2), arranged in a semi-circle, all feeding light to a single Kiwispec[8] high-resolution spectrograph (Barnes et al. 2012). In contrast, Northern MINERVA comprises of four 0.7 m PlaneWave CDK-700 telescopes (equivalent to a single 1.4 m diameter aperture versus a single 1.7 m aperture for MINERVA-Australis). The additional two telescopes in the MINERVA-Australis array provide us with 1.5× the collecting area and $\sim 1.2\times$ increase in S/N over Northern MINERVA. The PlaneWave CDK-700 telescope has a compact design that is 2.4 m tall when pointed at zenith and a radius of maximum extent of 1.5 m. The telescopes use a corrected Dall-Kirkham optical setup to remove off-axis coma, astigmatism, and field curvature. Over a three-minute interval, the telescopes have a pointing accuracy of 10″ RMS, pointing precision of 2″, and a tracking accuracy of 1″. The telescopes are controlled through a PWI interface. They also have a very fast slew rate of 15° per second, enabling the telescopes to slew between any two points on the sky within 10 seconds. For a complete discussion of the PlaneWave CDK-700 telescopes hardware and specifications, we refer the reader to the Northern MINERVA facility publication, Swift et al. (2015).

[6] This time excludes additional factors like unusually high humidity, dust storms, and maintenance.
[7] http://planewave.com/products-page/cdk700, three installed as of 30 September 2018
[8] https://www.kiwistaroptics.com/

Figure 2. Top: The MINERVA-Australis PlaneWave CDK-700 telescope inside an AstroHaven Enterprises Dome. Bottom: Schematic of the PlaneWave CDK-700 telescope obtained from the PlaneWave website.

Here we provide a summary of the important aspects of the telescopes and list the specifications in Table 1.

Figure 3. AstroHaven Enterprises dome housing a single PlaneWave CDK-700 Telescope.

Each of the PlaneWave CDK-700 telescopes is housed in its own AstroHaven Enterprises 12.5 ft (3.81 m) diameter dome[9], as shown in Figure 3. The dome is designed for remote and robotic operations from anywhere in the world. It can fully open, giving full access to the sky, and can achieve thermal equilibrium very rapidly, reducing the effects of "dome seeing". The dome can also open rapidly, in approximately 20 s, with each hemisphere opening independently. In contrast, the Northern MINERVA uses an "Aqawan" enclosure that was developed by Las Cumbres Observatory. A rectangular Aqawan can house two PlaneWave CDK-700 telescopes whereas each AstroHaven dome for MINERVA-Australis houses one Planewave telescope that can be independently operated.

The AstroHaven domes are powered by 240V/15A three phase power that is converted to 24V DC within its control panel and the telescopes by a 240V/10A power supply. This is then connected to an internal uninterruptible power supply (UPS) and stand-by generator, ensuring the dome can close if

[9] https://www.astrohaven.com/

Table 1. CDK-700 Specifications

Optical System	
Optical Design	Corrected Dall-Kirkham (CDK)
Aperture	700 mm (27.56 in)
Focal Length	4540 mm
Focal Ratio	6.5
Central Obscuration	47% primary diameter
Back Focus	305 mm from mounting surface
Focus Position	Nasmyth (dual)
Dimensions	93.73″ H × 43.25″ W × 39″ D
Weight	1200 lbs
Optical Performance	1.8 μm RMS spot size on axis
Image Scale	22 μm per arcsecond
Optimal Field of View	70 mm (0.86 degrees)
Fully Baffled Field	60 mm
Mechanical Structure	
Mount	Altitude-Azimuth
Fork	Monolithic U-shaped fork arm
Azimuth Bearing	20 in diameter thrust bearing
Altitude Bearing	2 × 8.5 in OD ball bearings
Optical Tube	Dual truss structure
Motion Control	
Motors	Direct drive, 3 phase axial flux torque motor
Encoders	Stainless steel encoder tape with 81 mas resolution
Motor Torque	$\sim$ 35 ft-lbs
Slew Rate	15° s^{-1}
System Performance	
Pointing Accuracy	10″ RMS
Pointing Precision	2″ RMS
Tracking Accuracy	1″ RMS over 3 minutes
Field De-Rotator	3 μm peak-to-peak 35 mm off axis over 1 hr

the site loses power and we can cease observing until power is restored. Communication to the domes are established by a TCP/IP interface and are controlled through ASCII string commands. We are

currently in the process of implementing an automated dome closure protocol in case communication is lost to the domes and telescopes for remote observing carried out in the future.

A web camera is situated inside each of the domes to provide a live video feed to the user. A weather station is located approximately 10 m to the north of the MINERVA-Australis building that provides real-time temperature, humidity, wind speed, and wind direction measurements. In addition, it also has a rain sensor that will alert the user to rain and send a signal to the dome control to close up the dome.

3.2. *Spectrograph*

All of the telescopes in the MINERVA-Australis array simultaneously feed a single Kiwispec R4-100 high-resolution spectrograph (Barnes et al. 2012) via fibre optic cables. The specifications for the spectrograph are provided in Table 2. The spectrograph is bench-mounted and housed in an insulated, environmentally controlled enclosure. Kiwispec uses an R4 echelle for the primary dispersion while a VPH grism is used for the cross-dispersion. The fibres are aligned in the cross-dispersion direction of the spectrometer that form seven individual echelle traces that are imaged on a 2k×2k detector. The detector has a wavelength coverage from 500 to 630 nm over from 26 echelle orders with a resolution of $R \approx 80,000$.

We currently use 50μm circular fibre cables with a 70μm cladding diameter that are butt-coupled to 50μm circulur fibres and a numerical aperture of 0.22 to feed scrambled light to the spectrograph. The 6 science fibres are bracketed by two additional calibration fibre that provides a simultaneous and stable Thorium-Argon wavelength calibration source. Octagonal fibres will replace the circular fibres in the final configuration of the instrument by mid 2019. Northern MINERVA in contrast uses octagonal fibres and has four science fibres for the four telescopes in the array. It also use an Iodine absorption cell placed in the light path instead of a Thorium-Argon lamp for wavelength calibration source. We chose to use Thorium-Argon as it provides good radial velocity precision (< 1 m s^{-1}, Mayor et al. 2003) without sacrificing the overall throughput of the system nor contaminating the spectra with Iodine absorption lines. More details on the commissioning and performance of the MINERVA-Australis Kiwispec spectrograph will be presented in a follow-up paper.

Table 2. KiwiSpec R4-100 Specifications

Characteristics	
Spectral Resolution	80,000
Wavelength Range	500 nm – 630 nm
Echelle Orders	26
Detector Size	2k×2k
Cross-disperser	Anamorphic VPH grisms
Beam diameter	100mm (at echelle grating), 33mm (at cross-disperser)
Main fibres	8× 50μm circular fibres (6 science and 2 calibration)
Average sampling	3.5 pixel per FWHM
Calibration	Simultaneous ThAr lamp
Environment for main optics	Vacuum operation, 1mK temperature stability
Environment for camera optics	Pressure sealed operation, 20mK temperature stability
Long-term instrument stability	Goal of 1 m s^{-1}

3.3. *Photometric Camera*

The MINERVA-Australis telescopes can each be equipped with an Andor iKon-L 936 camera[10], the specifications are provided in Table 3. Switching between our standard spectroscopic mode to the photometric observing mode is done through a simple flipping of the telescope's M3 mirror in the PWI software interface to direct stellar light to the imagining camera instead of the fibre that feeds the KiwiSpec spectrograph.

As of 2018 September, one photometric camera is present, on Telescope 1. Further cameras will be acquired subject to funding. The camera consists of 2048 × 2048 square 13.5μm pixels that provides an on-sky field of view of 20.9′, contain a deep depletion sensor with fringe suppression (BR-DD), and have a wide band (BV) coating. The deep depletion sensor enables the camera to be sensitive to light out to the near-infrared (1μm) for precision photometry. The cameras are also equipped

[10] https://andor.oxinst.com/products/ikon-xl-and-ikon-large-ccd-series/ikon-l-936

with a five-stage thermo-electric cooling system that allows the sensor to be cooled down to -100° C, keeping dark current to a minimum, without having to use liquid nitrogen.

Each telescope uses an Apogee AFW50-7s filter wheel, with second generation Sloan *g'*, *r'*, *i'*, *z'* filters; Johnson U, B, V, R, and I filters; and narrow band Hα filter. We chose these standard sets of filters to provide us with flexibility for our transit observations whilst observing in variable conditions and for our other auxiliary programs.

The Sloan *r'* filter is used for most transit photometric observations. For the transit observations of WASP-2b, WASP-44b, and WASP-45b, we used the *r'* filter. This filter provides good throughput whilst minimising atmospheric extinction effects. We used the *z'* band filter for observing the transit of HD 189733b since the star is quite bright ($V = 7.6$) and the quantum efficiency of our camera is a factor of 2 below peak. The *z'* filter is suitable for observing bright targets without reaching the non-linearity point or pixel saturation level for the detector at reasonable exposure lengths.

To obtain high precision photometry at high cadence with reasonably short readout times, our observations are carried out using the 1.0 MHz pixel readout mode. The total readout time for the detector in this mode is ~ 4 s with a readout noise of 22.2 e^{-}.

3.4. *Control Building*

Whilst Minerva-Australis is primarily designed for automated observing, it can be controlled both on site and remotely. The $2 million control facility features a purpose-built class 100,000 clean room that houses the spectrograph, with the critical components inside a vacuum chamber and thermally stabilized to ± 0.01 K. Additionally, it contains a UPS room where power for the entire Minerva-Australis facility is routed through for an uninterruptible power supply and a control room that houses the computers and network equipment.

4. FIRST SCIENCE RESULTS WITH MINERVA-AUSTRALIS

Whilst the primary focus of Minerva-Australis will be the radial velocity follow-up of transiting planet candidates found by *TESS*, five secondary photometric science goals include: photometric

Table 3. Andor iKon-L DR-DD Specifications

Characteristics	
Detector Size	2k×2k
Pixel Size	$13.5 \times 13.5\,\mu$m
Image area	27.6×27.6 mm
On-sky FOV	$20.9'$
Pixel well depth	150,000 e^-
Operating Temperature	$-100\,^\circ$C
Dark current (e^-/pixel/sec)	0.0003
Pixel Readout Rates	5.0, 3.0, 1.0, & 0.05 MHz
Read noise (e^-)	
0.05 MHz	8.7
1 MHz	22.2
3 MHz	40.2
5 MHz	70.3
Wavelength Regions (QE $\geq$ 50%)	430–975 nm
Peak QE	800 nm

follow-up of *TESS* and other transit survey planets to ensure that the ephemerides are up-to-date and accurate for future follow-up observations (e.g., Hoyer et al. 2016; Wang et al. 2018b), rule out potential false positives from nearby eclipsing binaries (NEBs, Collins et al. 2018; Ziegler et al. 2018), searching for transit timing variations (Malavolta et al. 2017; Saad-Olivera et al. 2017) and longer period planets (e.g., Otor et al. 2016; Almenara et al. 2018), following-up planets found by radial velocity observations from the AAPS (e.g., Tinney et al. 2011; Wittenmyer et al. 2014), and target-of-opportunity observations of high-priority Solar System occultation events (e.g., Sicardy et al. 2011a; Ortiz et al. 2012, 2017a). With this in mind, we conducted high-precision photometry observations of four known transiting exoplanets as part of the commissioning operations and to benchmark our photometric precision.

4.1. *High-Precision Photometry*

We carried out high-precision photometry for four known transiting planets exoplanets, WASP-2b, WASP-44b, WASP-45b, and HD 189733b using the first telescope that was installed at the

MINERVA-Australis site. Photometry was obtained using the Andor iKON-L camera and the Sloan r' (WASP-2b, WASP-44b, and WASP-45b) and z' (HD 189733b) filters as discussed in section 3.3. Maxim DL[11] was used to control the camera while the telescope was controlled through the PWI interface. No active guiding was used during the four transit observations. Active guiding is a feature that will be implemented soon and used for future transit photometry observations.

Series of calibration frames were obtained for each of the transit observations and standard photometric reduction procedures were followed to produce our calibrated science images. We then extracted photometry from our science images using the multi-aperture mode of AstroImageJ (Collins & Kielkopf 2013; Collins et al. 2017), which uses simple differential aperture photometry and sky-background subtraction. We then re-centered the apertures on individual stellar centroids in each image using the center-of-light method (Howell 2006). Details on the aperture size and the comparison stars used to produce the photometry are described in the respective subsections. The choice of comparison stars for each transit observation was based off of their counts, trends, and the amount of available stars in the image. The AstroImageJ differential photometry processor automatically removes any comparison star trends by comparing the flux in its aperture to the sum of the flux in all other comparison star apertures (Collins et al. 2017). To obtain the final de-trended light curves, we performed a linear detrending against the airmass using AstroImageJ.

We used the EXOFASTv2 Exoplanet model (Eastman 2017) in the Interactive Data Language (IDL[12]) to fit the transit light curves produced from our transit observations and to fit the radial velocity data for each of the planets we obtained from the literature. EXOFASTv2 uses a differential evolution Markov Chain Monte Carlo (MCMC) sampler to determine the best fit parameters and associated uncertainties from the resulting posterior distribution.

4.2. *Transit Observation of WASP-2b*

[11] http://diffractionlimited.com/product/maxim-dl/
[12] https://www.harrisgeospatial.com/Software-Technology/IDL

We observed the transit of WASP-2b (Collier Cameron et al. 2007), starting photometric observations on the evening of 2018 August 08 at approximately 10:30 UT, and continuing observing until 13:15 UT, obtaining 304 science frames with a cadence of 35 s. WASP-2 is a moderately faint ($V = 11.98$) K1V spectral type star hosting a hot Jupiter with an orbital period of $P = 2.15$ days (Collier Cameron et al. 2007). The sky was photometric with clear conditions during the transit observations and seeing of 3.5″.

From our calibrated science frames, we extracted differential photometry using the AstroImageJ reduction pipeline by first selecting an aperture of 15 pixels (9.15″) and a sky annulus with an inner radius of 30 pixels and an outer radius of 40 pixels around four stars, including WASP-2b.

Once we extracted the photometry, we removed systematic trends by performing a linear fit to the data with respect to the airmass and binned the data using a bin size of 4 (140 s) to produce the final light curve of WASP-2b. Figure 4 shows both the raw and detrended light curves. The RMS scatter of the residuals from the fit to our light curve is 0.95 mmag or 950 parts per million (ppm).

For the EXOFAST analysis, we employ Gaussian priors on the transit mid time (T_C), orbital period (P), radial velocity semi-amplitude (K), inclination angle (i), scaled semi-major axis (a/R_*), stellar surface gravity ($\log(g_*)$), stellar effective temperature (T_{eff}), and metallicity ([Fe/H]) taken from Collier Cameron et al. (2007). The priors on the quadratic stellar limb darkening coefficients u_1 and u_2 were informed from a/R_* and from the other transit parameters (using the look up tables in Claret & Bloemen 2011) that are tied to the Yonsei-Yale stellar models (Demarque et al. 2004). We placed uniform priors on the remaining free parameters, the systematic velocity (γ), the radial velocity slope term, baseline flux (F_0), and an error scaling for the uncertainties in the photometric and radial velocity data.

The best-fit transit model with the de-trended light curve and the residuals from the fit are shown in Figure 4. Table 4 list the resulting median parameter values and 1σ uncertainties.

Our results for WASP-2b are in general agreement with Collier Cameron et al. (2007). The mid-transit time we measured ($T_C = 2458339.00342^{+0.00028}_{-0.00027}$) is -0.00770 days (11.1 minutes) earlier than the predicted time of $T_C = 2458339.01112 \pm 0.0092$. This is in agreement with Collier Cameron et al.

(2007) predicted mid transit time when the accumulated uncertainty from 2020 orbital cycles since the last published ephemeris has been taken into account. Our measurement updates the published ephemeris, and extends the time baseline of WASP-2b transit photometry to approximately 12 years.

The orbital period we measured is $P = 2.152175^{+0.000012}_{-0.000011}$ days, which does not agree to within 3σ of the published period of $P = 2.152226 \pm 0.000004$ days (difference of 0.000051 days or $\sim 4\sigma$). The source of this discrepancy is not clear and Turner et al. (2017) found no evidence for transit timing variations. The results for our other parameters are in agreement with Collier Cameron et al. (2007).

4.3. *Transit Observation of WASP-44b*

Transit observation of WASP-44b were started on the night of 2018 August 07 at approximately 12:35 UT, nearly an hour before transit ingress. We continued to observe WASP-44b for about an hour after egress, observing until 16:10 UT, collecting 62 science frames with a cadence of 205 s. WASP-44b is a relatively faint ($V = 12.9$) G8V spectral type star that hosts a hot Jupiter with an orbital period of $P = 2.42$ days (Anderson et al. 2012). Our observations were done under clear skies and seeing of $4.1''$.

Photometry was extracted using the AstroImageJ reduction pipeline following the same procedure as detailed for WASP-2b. An aperture of 15 pixels ($9.15''$) and a sky annulus with an inner radius of 30 pixels and an outer radius of 40 pixels was chosen around our target and comparison stars, re-centering the apertures on individual stellar centroids in each image. We then removed systematic trends by performing a linear fit to the data with respect to the airmass to produce the final light curve of WASP-44b (Figure 5). The RMS scatter of the residuals from the fit to our light curve is 1.18 mmag (1180 ppm).

Gaussian priors were placed on the same model parameters as we used for WASP-2b and taken from Anderson et al. (2012). Uniform priors were placed on the remaining free parameters, the systematic velocity (γ), the radial velocity slope term, baseline flux (F_0), and an error scaling for the uncertainties in the photometric and radial velocity data.

The best fit transit model with the de-trended light curve and the residuals from the fit are shown in Figure 5. Table 5 list the resulting median parameter values and 1σ uncertainties.

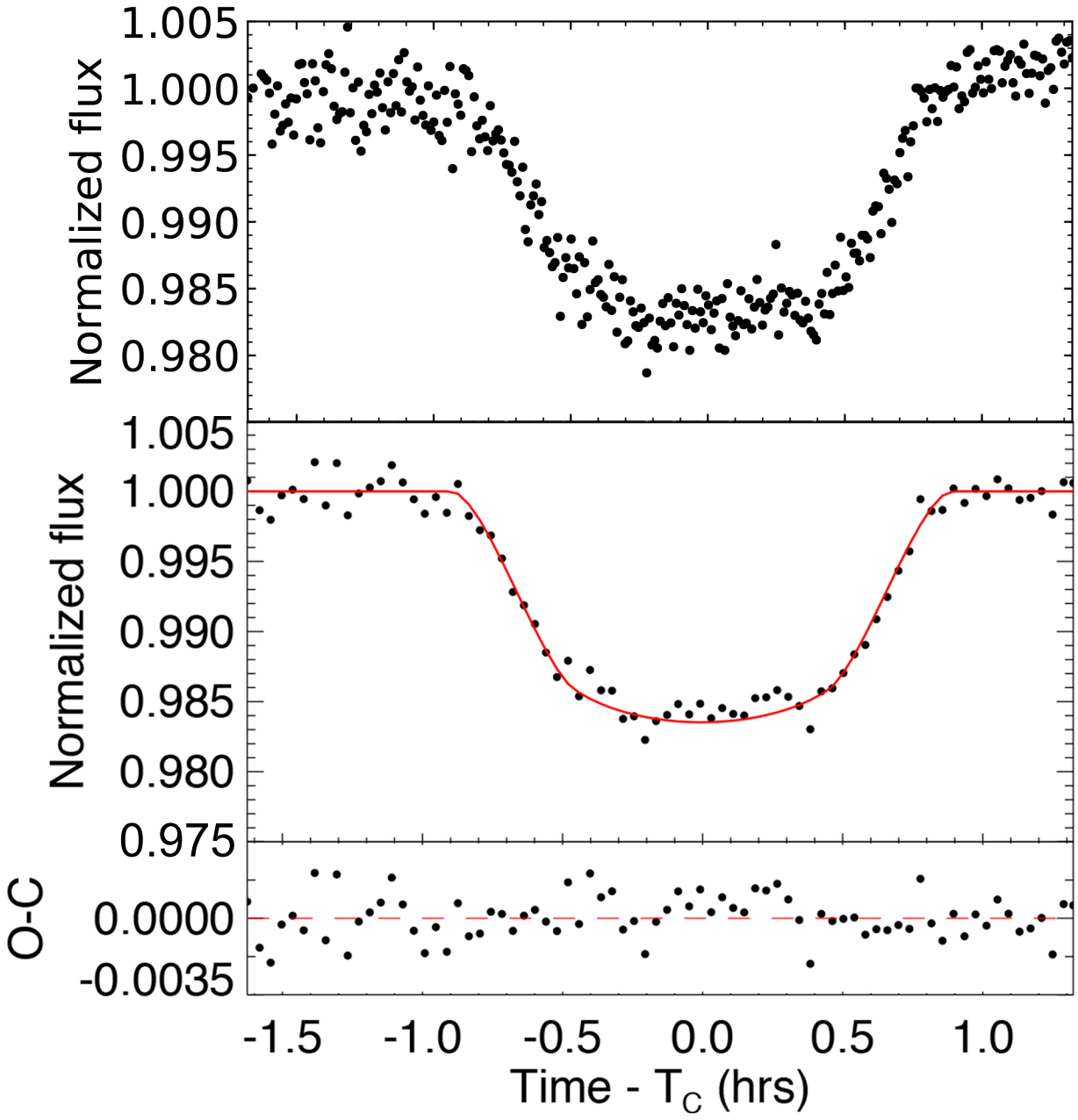

Figure 4. Transit light curve data for WASP-2b, top light curve normalized but not de-trended and the bottom one is normalized, de-trended, and binned with a best fit model over plotted. Bottom panel shows the residuals to the best fit model. T_C is the mid transit time.

Overall our results for WASP-44b are in good agreement with Anderson et al. (2012) to within 1σ. The mid transit time we measured ($T_C = 2458338.102384^{+0.000364}_{-0.000374}$) is 0.0093 days or 13.4 minutes later

Table 4. Median values and 68% confidence interval for WASP-2b

Parameter	Units	Value
Stellar Parameters:		
M_*	Mass ($M_\odot$)	$0.895^{+0.077}_{-0.072}$
R_*	Radius ($R_\odot$)	$0.866^{+0.031}_{-0.030}$
L_*	Luminosity ($L_\odot$)	$0.486^{+0.100}_{-0.087}$
[-0.5ex] ρ_*	Density (cgs)	1.94 ± 0.10
$\log(g_*)$	Surface gravity (cgs)	4.514 ± 0.018
T_{eff}	Effective temperature (K)	5180 ± 190
[Fe/H]	Metalicity	$0.12^{+0.21}_{-0.19}$
Planetary Parameters:		
P	Period (days)	$2.152175^{+0.000012}_{-0.000011}$
a	Semi-major axis (AU)	$0.03144^{+0.00088}_{-0.00087}$
M_P	Mass ($M_{\rm J}$)	$0.931^{+0.060}_{-0.058}$
R_P	Radius ($R_{\rm J}$)	$1.081^{+0.041}_{-0.040}$
ρ_P	Density (cgs)	$0.914^{+0.074}_{-0.071}$
$\log(g_P)$	Surface gravity	3.295 ± 0.023
T_{eq}	Equilibrium Temperature (K)	1311^{+52}_{-50}
$\langle F \rangle$	Incident flux (10^9 erg s^{-1} cm^{-2})	$0.670^{+0.110}_{-0.097}$
RV Parameters:		
K	RV semi-amplitude (m/s)	$157.0^{+4.7}_{-4.6}$
$M_P \sin i$	Minimum mass ($M_{\rm J}$)	$0.927^{+0.060}_{-0.057}$
M_P/M_*	Mass ratio	$0.000993^{+0.000042}_{-0.000039}$
γ	Systemic velocity (m/s)	$-27872.3^{+6.0}_{-6.1}$
Primary Transit Parameters:		
T_C	Time of transit ($\rm BJD_{TDB}$)	$2458339.00342^{+0.00028}_{-0.00027}$
R_P/R_*	Radius of planet in stellar radii	$0.12831^{+0.00098}_{-0.00100}$
a/R_*	Semi-major axis in stellar radii	$7.81^{+0.13}_{-0.14}$
u_1	linear limb-darkening coeff	0.523 ± 0.063
u_2	quadratic limb-darkening coeff	$0.174^{+0.059}_{-0.058}$
i	Inclination (degrees)	$84.49^{+0.17}_{-0.18}$
b	Impact Parameter	$0.749^{+0.012}_{-0.013}$
δ	Transit depth	0.01646 ± 0.00025
T_{FWHM}	FWHM duration (days)	0.0569 ± 0.0010
τ	Ingress/egress duration (days)	$0.01761^{+0.00080}_{-0.00074}$
T_{14}	Total duration (days)	$0.07451^{+0.00099}_{-0.00094}$
Secondary Eclipse Parameters:		
T_S	Time of eclipse ($\rm BJD_{TDB}$)	$2458340.07950^{+0.00028}_{-0.00027}$

than the predicted time of of $T_C = 2458338.09307 \pm 0.01040$, but is in agreement with Anderson et al.

(2012) when the accumulated uncertainties from 1198 orbital cycles since the last ephemeris have been taken into account for the mid transit time uncertainty. Thus our measurements do agree with the predicted time and suggest that there is no significant deviation in the transit time. We have now provided an update to the published ephemeris that extends the time baseline of WASP-44b transit photometry to approximately 8 years.

4.4. *Transit Observation of WASP-45b*

On the night of 2018 August 08, we observed another transiting planet, WASP-45b, after observations of WASP-2b had finished. For this transit, observing commenced at 13:55 UT (just over an hour before ingress) and continued until 17:20 UT ($\sim$ 2 hr after egress). In total we obtained 219 science frames with a cadence of 55 s. WASP-45 is a moderately faint ($V = 12.0$) K2V spectral type star hosting a hot Jupiter with an orbital period of $P = 3.13$ days (Anderson et al. 2012). WASP-45b was observed under similarly clear skies, however, the seeing was worse (6.1″).

We followed the same overall procedure for extracting photometry as described in Section 4.1. An aperture of 15 pixels (9.15″) and a sky annulus with an inner radius of 30 pixels and an outer radius of 40 pixels was chosen around our target and nine comparison stars for deriving the photometry. The resultant de-trended light curve as shown in Figure 6. The RMS scatter from our best fit light curve model is 1.2 mmag (1200 ppm).

Gaussian priors were placed on the same model parameters for WASP-45b as was done for the analysis of the previous two planets. The prior values were taken from Anderson et al. (2012). Uniform priors were used on the remaining free parameters.

The best fit transit model with the de-trended light curve and the residuals from the fit are shown in Figure 6. Table 6 list the resulting median parameter values and 1σ uncertainties.

Our results for WASP-45b are generally in good agreement with Anderson et al. (2012). The mid transit time we measured ($T_C = 2458339.143039^{+0.000312}_{-0.000310}$) is -0.00942 days (-13.6 minutes) earlier than the predicted time of $T_C = 2458339.15246 \pm 0.00058$ from Anderson et al. (2012) but is in agreement with their result when the uncertainty on the orbital period is taken into account after

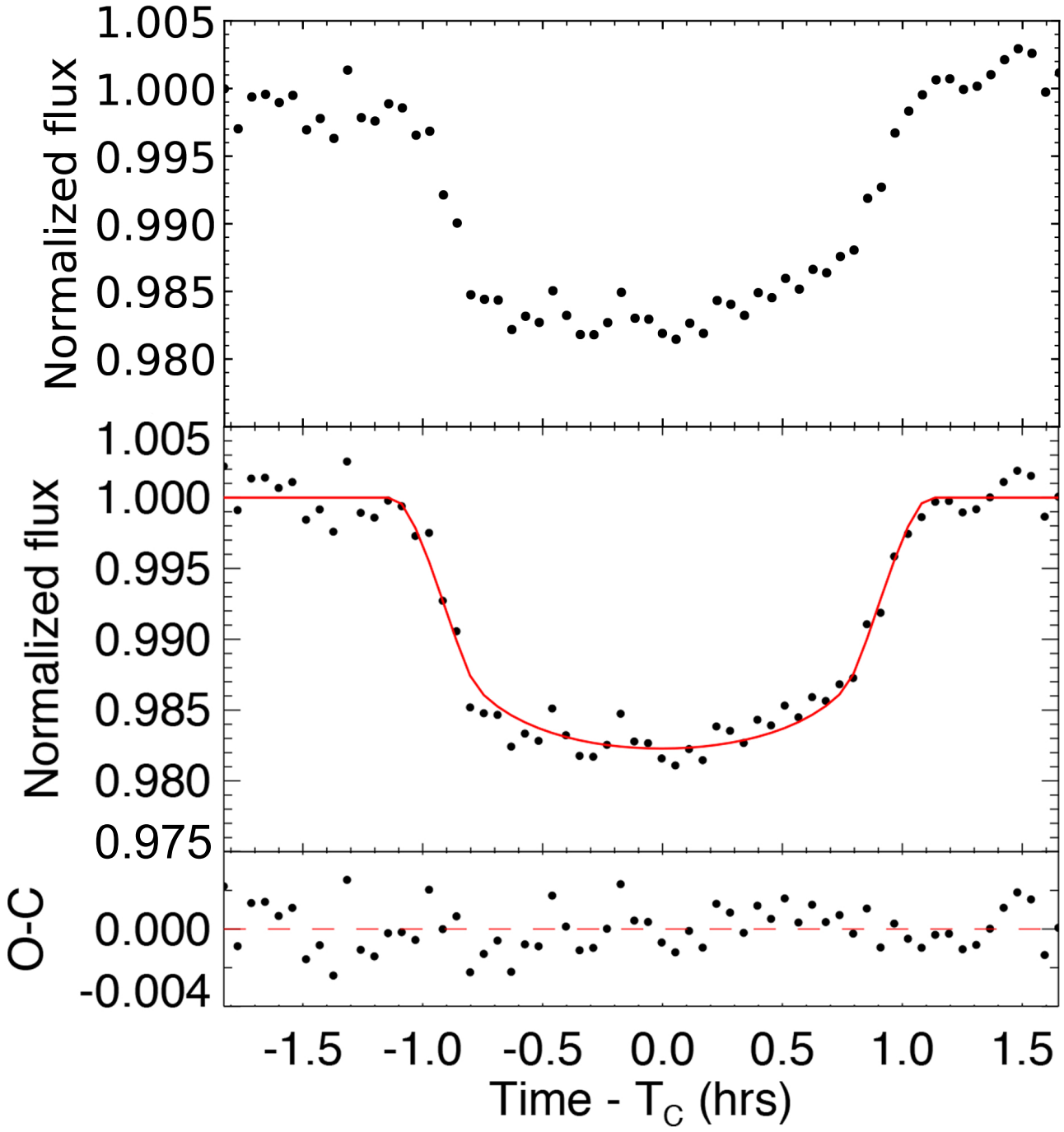

Figure 5. Same as Figure 4, but for the light curve of WASP-44b.

927 orbital periods. Our transit observation now extends the published ephemeris to a time baseline of approximately 8 years.

Table 5. Median values and 68% confidence interval for WASP-44b

Parameter	Units	Value
Stellar Parameters:		
M_*	Mass ($M_\odot$)	$0.935^{+0.054}_{-0.052}$
R_*	Radius ($R_\odot$)	$0.906^{+0.053}_{-0.050}$
L_*	Luminosity ($L_\odot$)	$0.6342^{+0.100}_{-0.087}$
ρ_*	Density (cgs)	$1.77^{+0.30}_{-0.25}$
$\log(g_*)$	Surface gravity (cgs)	$4.494^{+0.044}_{-0.044}$
T_{eff}	Effective temperature (K)	5420 ± 100
[Fe/H]	Metallicity	-0.003 ± 0.100
Planetary Parameters:		
P	Period (days)	2.423804 ± 0.000008
a	Semi-major axis (AU)	0.03453 ± 0.00065
M_P	Mass (M_J)	$0.870^{+0.063}_{-0.062}$
R_P	Radius (R_J)	$1.1000^{+0.081}_{-0.076}$
ρ_P	Density (cgs)	$0.811^{+0.188}_{-0.155}$
$\log(g_P)$	Surface gravity	3.25 ± 0.06
T_{eq}	Equilibrium Temperature (K)	1337^{+43}_{-42}
$\langle F \rangle$	Incident flux (10^9 erg s^{-1} cm^{-2})	$0.726^{+0.098}_{-0.087}$
RV Parameters:		
K	RV semi-amplitude (m/s)	138^{+8}_{-9}
$M_P \sin i$	Minimum mass (M_J)	$0.869^{+0.063}_{-0.062}$
M_P/M_*	Mass ratio	0.00089 ± 0.00006
γ	Systemic velocity (m/s)	-4044 ± 6
Primary Transit Parameters:		
T_C	Time of transit ($\mathrm{BJD_{TDB}}$)	$2458338.102384^{+0.000364}_{-0.000374}$
R_P/R_*	Radius of planet in stellar radii	0.1248 ± 0.0023
a/R_*	Semi-major axis in stellar radii	$8.20^{+0.43}_{-0.42}$
u_1	linear limb-darkening coeff	0.449 ± 0.051
u_2	quadratic limb-darkening coeff	$0.231^{+0.051}_{-0.052}$
i	Inclination (degrees)	$86.21^{+0.68}_{-0.64}$
b	Impact Parameter	$0.541^{+0.061}_{-0.074}$
δ	Transit depth	0.0156 ± 0.0006
T_{FWHM}	FWHM duration (days)	$0.0790^{+0.0012}_{-0.0011}$
τ	Ingress/egress duration (days)	$0.0141^{+0.0018}_{-0.0016}$
T_{14}	Total duration (days)	$0.0932^{+0.0020}_{-0.0019}$
Secondary Eclipse Parameters:		
T_S	Time of eclipse ($\mathrm{BJD_{TDB}}$)	$2458339.314286^{+0.000365}_{-0.000374}$

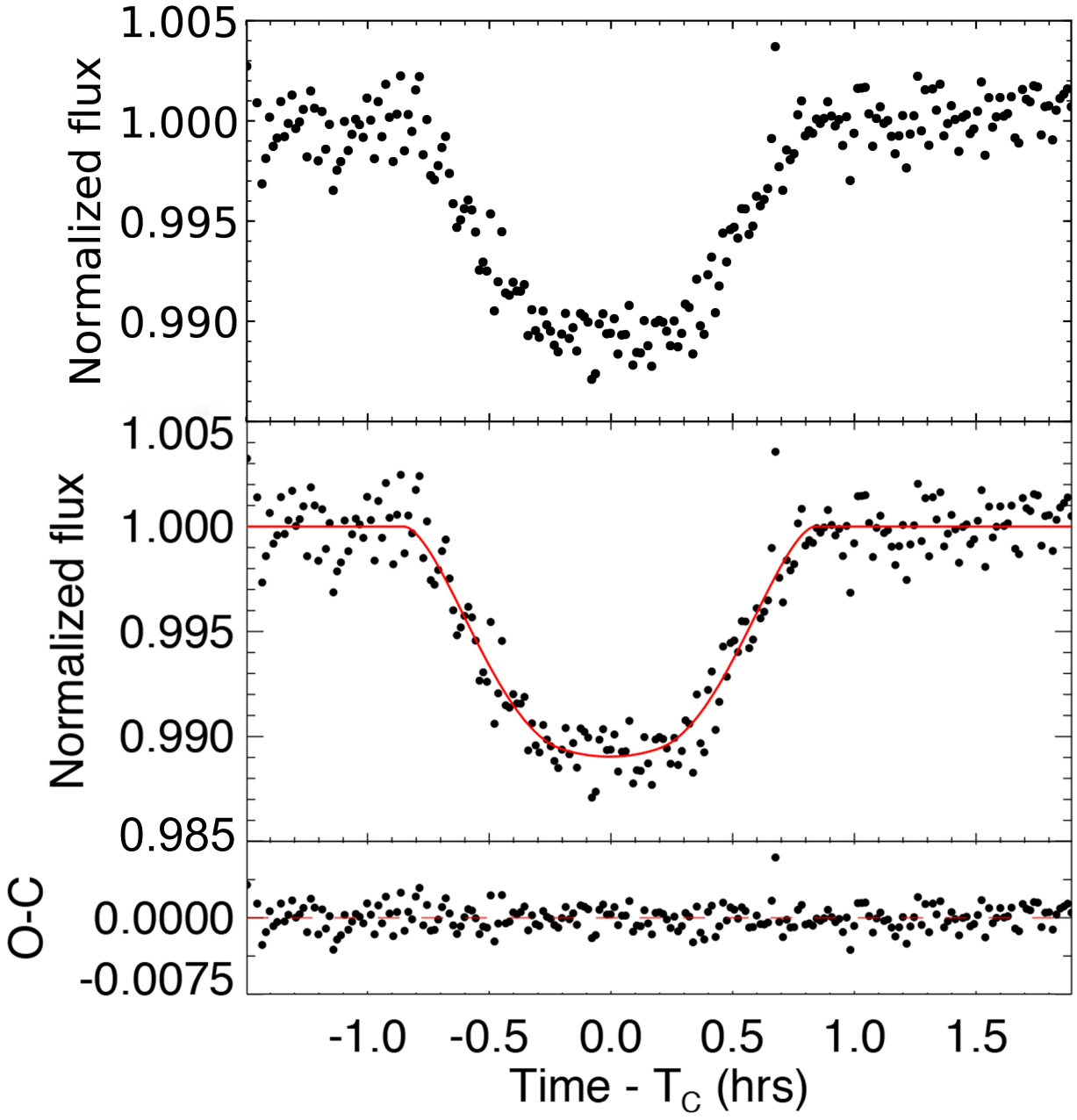

Figure 6. Same as Figure 4, but for the light curve of WASP-45b.

There are 1 to 1.5σ discrepancies seen in T_{14}, a/R_*, i, M_*, R_*, and R_P. The origin of this discrepancy is not understood but could potentially be from stellar activity as Anderson et al. (2012) reported WASP-45 to be chromospherically active.

Table 6. Median values and 68% confidence interval for WASP-45b

Parameter	Units	Value
Stellar Parameters:		
M_*	Mass ($M_\odot$)	$0.850^{+0.076}_{-0.070}$
R_*	Radius ($R_\odot$)	$0.855^{+0.039}_{-0.038}$
L_*	Luminosity ($L_\odot$)	$0.4618^{+0.1077}_{-0.0927}$
ρ_*	Density (cgs)	$1.92^{+0.17}_{-0.17}$
$\log(g_*)$	Surface gravity (cgs)	$4.503^{+0.027}_{-0.029}$
T_{eff}	Effective temperature (K)	5150 ± 200
[Fe/H]	Metallicity	-0.03 ± 0.20
Planetary Parameters:		
P	Period (days)	3.126089 ± 0.000003
a	Semi-major axis (AU)	$0.03963^{+0.00114}_{-0.00112}$
M_P	Mass ($M_{\rm J}$)	$0.964^{+0.058}_{-0.056}$
R_P	Radius ($R_{\rm J}$)	$0.946^{+0.058}_{-0.051}$
ρ_P	Density (cgs)	1.418 ± 0.207
$\log(g_P)$	Surface gravity	3.43 ± 0.04
T_{eq}	Equilibrium Temperature (K)	1153 ± 50
$\langle F \rangle$	Incident flux (10^9 erg s^{-1} cm^{-2})	$0.400^{+0.074}_{-0.065}$
RV Parameters:		
K	RV semi-amplitude (m/s)	149 ± 2
$M_P \sin i$	Minimum mass ($M_{\rm J}$)	$0.961^{+0.058}_{-0.055}$
M_P/M_*	Mass ratio	$0.00108^{+0.00004}_{-0.00003}$
γ	Systemic velocity (m/s)	4550 ± 2
Primary Transit Parameters:		
T_C	Time of transit ($\rm BJD_{TDB}$)	$2458339.143039^{+0.000312}_{-0.000310}$
R_P/R_*	Radius of planet in stellar radii	$0.1137^{+0.0029}_{-0.0022}$
a/R_*	Semi-major axis in stellar radii	$9.97^{+0.30}_{-0.31}$
u_1	linear limb-darkening coeff	0.511 ± 0.070
u_2	quadratic limb-darkening coeff	$0.192^{+0.060}_{-0.062}$
i	Inclination (degrees)	$85.02^{+0.20}_{-0.22}$
b	Impact Parameter	$0.866^{+0.013}_{-0.012}$
δ	Transit depth	$0.0129^{+0.0007}_{-0.0005}$
T_{FWHM}	FWHM duration (days)	$0.0444^{+0.0023}_{-0.0040}$
τ	Ingress/egress duration (days)	$0.0256^{+0.0046}_{-0.0027}$
T_{14}	Total duration (days)	0.0701 ± 0.0013
Secondary Eclipse Parameters:		
T_S	Time of eclipse ($\rm BJD_{TDB}$)	$2458340.706084^{+0.000312}_{-0.000311}$

4.5. *Transit Observation of HD 189733b*

We observed the transit of HD 189733b on the night of UT 2018 August 04 with photometric observations starting at approximately 10:00UT (about 1 hour before ingress). We continued observing the target until approximately 30 minutes after egress (13:15UT), obtaining 517 observations with a cadence of ~ 7 s. HD 189733 is a very bright ($V = 7.6$) K2 spectral type star hosting a hot Jupiter with an orbital period of $P = 2.22$ (Bouchy et al. 2005). The observations were conducted under clear skies and seeing of 2.6″.

Following the procedure described in Section 4.1, we extracted photometry using the AstroImageJ by first selecting an aperture of 20 pixels (12.3″) and a sky annulus with an inner radius of 35 pixels and an outer radius of 45 pixels around 14 stars, including HD 189733. The resultant light curve of HD 189733b is shown in (Figure 7). The RMS scatter of the residuals from the fit to our light curve is 5.2 mmag (5200 ppm).

Gaussian priors were placed on the same model parameters for the HD 189733b analysis as was done for the previous systems while uniform priors were placed on the remaining free parameters. The prior values were taken from Bouchy et al. (2005) and Bakos et al. (2006).

The best fit transit model with the de-trended light curve and the residuals from the fit are shown in Figure 7. Table 7 list the resulting median parameter values and 1σ uncertainties.

Our results for HD 189733b are in good agreement with Bouchy et al. (2005); Bakos et al. (2006); Southworth (2010); Baluev et al. (2015). The mid transit time we measured ($T_C = 2458334.990899^{+0.000726}_{-0.000781}$) is -0.0021 days (-3.0 minutes) earlier than the predicted time of $T_C = 2458334.9930000 \pm 0.0000088$ from Baluev et al. (2015) but is in agreement with their result when the uncertainty on the orbital period is taken into account after 1974 orbital periods. HD 189733b now has an ephemeris baseline of approximately 13 years. There are 1 to 1.5σ discrepancies seen in R_P, b, and R_* compared to the literature values (Bouchy et al. 2005; Bakos et al. 2006; Southworth 2010; Baluev et al. 2015).

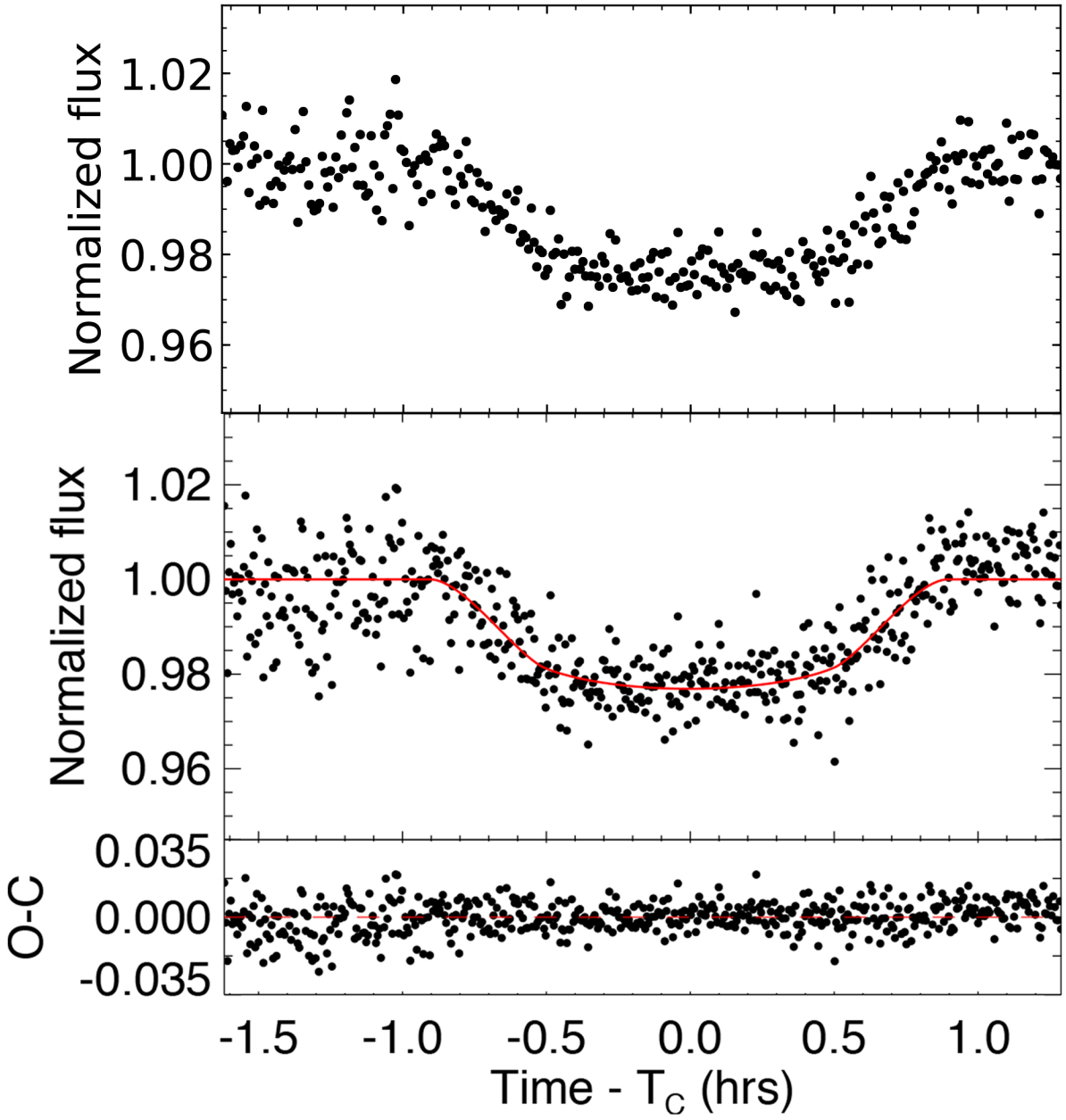

Figure 7. Same as Figure 4, but for the light curve of HD 189733b.

Table 7. Median values and 68% confidence interval for HD 189733b

Parameter	Units	Value
Stellar Parameters:		
M_*	Mass ($M_\odot$)	$0.812^{+0.041}_{-0.038}$
R_*	Radius ($R_\odot$)	$0.765^{+0.019}_{-0.018}$
L_*	Luminosity ($L_\odot$)	$0.3424^{+0.0182}_{-0.0169}$
ρ_*	Density (cgs)	$2.56^{+0.13}_{-0.13}$
$\log(g_*)$	Surface gravity (cgs)	$4.580^{+0.016}_{-0.016}$
T_{eff}	Effective temperature (K)	5050 ± 20
[Fe/H]	Metallicity	-0.03 ± 0.10
Planetary Parameters:		
P	Period (days)	$2.218577^{+0.000009}_{-0.000010}$
a	Semi-major axis (AU)	$0.03106^{+0.00051}_{-0.00049}$
M_P	Mass ($M_{\rm J}$)	$1.166^{+0.052}_{-0.049}$
R_P	Radius ($R_{\rm J}$)	1.119 ± 0.038
ρ_P	Density (cgs)	$1.031^{+0.106}_{-0.090}$
$\log(g_P)$	Surface gravity	3.36 ± 0.03
T_{eq}	Equilibrium Temperature (K)	1209 ± 11
$\langle F \rangle$	Incident flux (10^9 erg s^{-1} cm^{-2})	$0.484^{+0.018}_{-0.017}$
RV Parameters:		
K	RV semi-amplitude (m/s)	208 ± 6
$M_P \sin i$	Minimum mass ($M_{\rm J}$)	$1.163^{+0.052}_{-0.049}$
M_P/M_*	Mass ratio	0.00137 ± 0.00005
γ	Systemic velocity (m/s)	-2204^{+10}_{-11}
Primary Transit Parameters:		
T_C	Time of transit ($\rm BJD_{TDB}$)	$2458334.990899^{+0.000726}_{-0.000781}$
R_P/R_*	Radius of planet in stellar radii	$0.1504^{+0.0038}_{-0.0039}$
a/R_*	Semi-major axis in stellar radii	8.73 ± 0.15
u_1	linear limb-darkening coeff	$0.545^{+0.048}_{-0.050}$
u_2	quadratic limb-darkening coeff	0.185 ± 0.051
i	Inclination (degrees)	$85.69^{+0.095}_{-0.097}$
b	Impact Parameter	$0.656^{+0.014}_{-0.015}$
δ	Transit depth	$0.0226^{+0.0011}_{-0.0012}$
T_{FWHM}	FWHM duration (days)	$0.0602^{+0.0019}_{-0.0018}$
τ	Ingress/egress duration (days)	0.0165 ± 0.0006
T_{14}	Total duration (days)	0.0767 ± 0.0018
Secondary Eclipse Parameters:		
T_S	Time of eclipse ($\rm BJD_{TDB}$)	$2458336.100188^{+0.000724}_{-0.000780}$

5. CONCLUSIONS AND FUTURE WORK

We have built a dedicated observatory for high-precision photometric and spectroscopic observations of exoplanetary systems, primarily in support of the NASA *TESS* mission. MINERVA-Australis is the only Southern Hemisphere facility with such capabilities that is fully dedicated to *TESS* follow-up.

In this work, we have presented initial photometric science demonstration results. Based on these results, we expect to contribute high precision (≤ 1.0 mmag) photometry for TESS targets brighter than $V = 13$ with exposures of under 5 minutes. This is comparable to the MINERVA North photometric commissioning results (Swift et al. 2015) and to other ground-based follow-up programs such as HATSouth carried out on the Las Cumbres Observatory (LCO) 1 m telescopes, Danish (DK) 1.54 m telescope, Chilean-Hungarian Automated Telescope (CHAT) 0.7 m telescope, and Perth Exoplanet Survey Telescope (PEST) 0.3 m telescope that obtained photometric precision of 0.9–3.0 mmag for $V \leq 13$ targets (e.g., see, Hartman et al. 2019). At the time of writing, the KiwiSpec spectrograph is being commissioned. In a forthcoming paper (Wright et al., in prep), we will fully describe the acquisition and analysis of spectroscopic data at MINERVA-Australis, and we will present data demonstrating our radial velocity precision on standard stars and known exoplanets.

We are also in the process of enabling fully autonomous operations of the telescope array by customising the existing automation software, MINERVA Robotic Software (MRS, Swift et al. 2015), developed for the MINERVA North array to suit our specific scientific goals and operational requirements.

In future, we anticipate adding very high-cadence photometric capability, as each telescope can rapidly switch between photometric and spectroscopic modes via use of the two Nasmyth ports. With photometric cadence of up to 20 Hz, MINERVA-Australis will be able to capture occultation events of small Solar system bodies (e.g. Braga-Ribas et al. 2014b; Ortiz et al. 2015, 2017b), allowing us to pursue time-critical target-of-opportunity research, in addition to pursuing our core goals in exoplanetary science.

6. ACKNOWLEDGEMENTS

This research was supported by the Australian Government through the Australian Research Council's Discovery Projects funding scheme (project DP180100972). MINERVA-Australis hardware is funded in part by the Australian government through the Australian Research Council, LIEF grants LE160100001. We acknowledge support from the Mount Cuba Astronomical Foundation. Zhang is also grateful to the support from the Natural Science Foundation of China (NSFC grants 11673011, 11333002). Plavchan acknowledges support from the the National Science Foundation (Astronomy and Astrophysics grant 1716202) and George Mason University start-up funds.

REFERENCES

Addison, B. C., Wang, S., Johnson, M. C., et al. 2018, ArXiv e-prints. https://arxiv.org/abs/1809.00314

Albrecht, S., Winn, J. N., Marcy, G. W., et al. 2013, ApJ, 771, 11, doi: 10.1088/0004-637X/771/1/11

Almenara, J. M., Díaz, R. F., Hébrard, G., et al. 2018, A&A, 615, A90, doi: 10.1051/0004-6361/201732500

Anderson, D. R., Collier Cameron, A., Gillon, M., et al. 2012, MNRAS, 422, 1988, doi: 10.1111/j.1365-2966.2012.20635.x

Bailes, M., Lyne, A. G., & Shemar, S. L. 1991, Nature, 352, 311, doi: 10.1038/352311a0

Bakos, G. Á., Knutson, H., Pont, F., et al. 2006, ApJ, 650, 1160, doi: 10.1086/506316

Bakos, G. Á., Torres, G., Pál, A., et al. 2010, ApJ, 710, 1724, doi: 10.1088/0004-637X/710/2/1724

Baluev, R. V., Sokov, E. N., Shaidulin, V. S., et al. 2015, MNRAS, 450, 3101, doi: 10.1093/mnras/stv788

Barnes, S. I., Gibson, S., Nield, K., & Cochrane, D. 2012, in Proc. SPIE, Vol. 8446, Ground-based and Airborne Instrumentation for Astronomy IV, 844688

Barragán, O., Gandolfi, D., Dai, F., et al. 2018, A&A, 612, A95, doi: 10.1051/0004-6361/201732217

Bayliss, D., Zhou, G., Penev, K., et al. 2013, AJ, 146, 113, doi: 10.1088/0004-6256/146/5/113

Bodenheimer, P., Hubickyj, O., & Lissauer, J. J. 2000, Icarus, 143, 2, doi: 10.1006/icar.1999.6246

Boisse, I., Bouchy, F., Hébrard, G., et al. 2011, A&A, 528, A4, doi: 10.1051/0004-6361/201014354

Bouchy, F., Udry, S., Mayor, M., et al. 2005, A&A, 444, L15, doi: 10.1051/0004-6361:200500201

Braga-Ribas, F., Sicardy, B., Ortiz, J. L., et al. 2014a, Nature, 508, 72, doi: 10.1038/nature13155

—. 2014b, Nature, 508, 72, doi: 10.1038/nature13155

Charbonneau, D., Brown, T. M., Latham, D. W., & Mayor, M. 2000, ApJL, 529, L45, doi: 10.1086/312457

Charbonneau, D., Berta, Z. K., Irwin, J., et al. 2009, Nature, 462, 891, doi: 10.1038/nature08679

Christiansen, J. L., Vanderburg, A., Burt, J., et al. 2017, AJ, 154, 122, doi: 10.3847/1538-3881/aa832d

Claret, A., & Bloemen, S. 2011, A&A, 529, A75, doi: 10.1051/0004-6361/201116451

Collier Cameron, A., Bouchy, F., Hébrard, G., et al. 2007, MNRAS, 375, 951, doi: 10.1111/j.1365-2966.2006.11350.x

Collins, K., & Kielkopf, J. 2013, AstroImageJ: ImageJ for Astronomy, Astrophysics Source Code Library. http://ascl.net/1309.001

Collins, K. A., Kielkopf, J. F., Stassun, K. G., & Hessman, F. V. 2017, AJ, 153, 77, doi: 10.3847/1538-3881/153/2/77

Collins, K. A., Collins, K. I., Pepper, J., et al. 2018, ArXiv e-prints. https://arxiv.org/abs/1803.01869

Crida, A., & Batygin, K. 2014, A&A, 567, A42, doi: 10.1051/0004-6361/201323292

Deleuil, M., Deeg, H. J., Alonso, R., et al. 2008, A&A, 491, 889, doi: 10.1051/0004-6361:200810625

Demarque, P., Woo, J.-H., Kim, Y.-C., & Yi, S. K. 2004, ApJS, 155, 667, doi: 10.1086/424966

Dong, S., Katz, B., & Socrates, A. 2014, ApJL, 781, L5, doi: 10.1088/2041-8205/781/1/L5

Dressing, C. D., & Charbonneau, D. 2013, ApJ, 767, 95, doi: 10.1088/0004-637X/767/1/95

Dumusque, X., Bonomo, A. S., Haywood, R. D., et al. 2014, ApJ, 789, 154, doi: 10.1088/0004-637X/789/2/154

Eastman, J. 2017, EXOFASTv2: Generalized publication-quality exoplanet modeling code, Astrophysics Source Code Library. http://ascl.net/1710.003

Faedi, F., Barros, S. C. C., Anderson, D. R., et al. 2011, A&A, 531, A40, doi: 10.1051/0004-6361/201116671

Fleming, S. W., Mahadevan, S., Deshpande, R., et al. 2015, AJ, 149, 143, doi: 10.1088/0004-6256/149/4/143

Ford, E. B., & Rasio, F. A. 2008, ApJ, 686, 621, doi: 10.1086/590926

Fressin, F., Torres, G., Charbonneau, D., et al. 2013, ApJ, 766, 81, doi: 10.1088/0004-637X/766/2/81

Gandolfi, D., Barragan, O., Livingston, J., et al. 2018, ArXiv e-prints. https://arxiv.org/abs/1809.07573

Gatewood, G. D. 1995, Ap&SS, 223, 91, doi: 10.1007/BF00989158

Gillon, M., Pont, F., Demory, B.-O., et al. 2007, A&A, 472, L13, doi: 10.1051/0004-6361:20077799

Hartman, J. D., Bakos, G. Á., Bayliss, D., et al. 2019, AJ, 157, 55, doi: 10.3847/1538-3881/aaf8b6

Haywood, R. D., Collier Cameron, A., Queloz, D., et al. 2014, MNRAS, 443, 2517, doi: 10.1093/mnras/stu1320

Howell, S. B. 2006, Handbook of CCD Astronomy (UK: Cambridge University Press)

Howell, S. B., Sobeck, C., Haas, M., et al. 2014, PASP, 126, 398, doi: 10.1086/676406

Hoyer, S., Pallé, E., Dragomir, D., & Murgas, F. 2016, AJ, 151, 137, doi: 10.3847/0004-6256/151/6/137

Huang, C. X., Burt, J., Vanderburg, A., et al. 2018, ArXiv e-prints. https://arxiv.org/abs/1809.05967

Jacob, W. S. 1855, MNRAS, 15, 228, doi: 10.1093/mnras/15.9.228

Johns, D., Marti, C., Huff, M., et al. 2018, ArXiv e-prints. https://arxiv.org/abs/1808.04533

Johnson, M. C., Cochran, W. D., Albrecht, S., et al. 2014, ApJ, 790, 30, doi: 10.1088/0004-637X/790/1/30

Jones, H. R. A., Butler, R. P., Tinney, C. G., et al. 2006, MNRAS, 369, 249, doi: 10.1111/j.1365-2966.2006.10298.x

Koch, D. G., Borucki, W. J., Basri, G., et al. 2010, ApJL, 713, L79, doi: 10.1088/2041-8205/713/2/L79

Lin, D. N. C., Bodenheimer, P., & Richardson, D. C. 1996, Nature, 380, 606, doi: 10.1038/380606a0

Lyne, A. G., & Bailes, M. 1992, Nature, 355, 213, doi: 10.1038/355213b0

Malavolta, L., Borsato, L., Granata, V., et al. 2017, AJ, 153, 224, doi: 10.3847/1538-3881/aa6897

Mayor, M., & Queloz, D. 1995, Nature, 378, 355, doi: 10.1038/378355a0

Mayor, M., Pepe, F., Queloz, D., et al. 2003, The Messenger, 114, 20

McLaughlin, D. B. 1924, ApJ, 60, doi: 10.1086/142826

Naoz, S., Farr, W. M., Lithwick, Y., Rasio, F. A., & Teyssandier, J. 2011, Nature, 473, 187, doi: 10.1038/nature10076

Ortiz, J. L., Sicardy, B., Braga-Ribas, F., et al. 2012, Nature, 491, 566, doi: 10.1038/nature11597

Ortiz, J. L., Duffard, R., Pinilla-Alonso, N., et al. 2015, A&A, 576, A18, doi: 10.1051/0004-6361/201424461

Ortiz, J. L., Santos-Sanz, P., Sicardy, B., et al. 2017a, Nature, 550, 219, doi: 10.1038/nature24051

—. 2017b, Nature, 550, 219, doi: 10.1038/nature24051

Oshagh, M., Triaud, A. H. M. J., Burdanov, A., et al. 2018, A&A, 619, A150, doi: 10.1051/0004-6361/201833709

Otor, O. J., Montet, B. T., Johnson, J. A., et al. 2016, AJ, 152, 165, doi: 10.3847/0004-6256/152/6/165

Pepper, J., Kuhn, R. B., Siverd, R., James, D., & Stassun, K. 2012, PASP, 124, 230, doi: 10.1086/665044

Pepper, J., Pogge, R. W., DePoy, D. L., et al. 2007, PASP, 119, 923, doi: 10.1086/521836

Pepper, J., Rodriguez, J. E., Collins, K. A., et al. 2017, AJ, 153, 215, doi: 10.3847/1538-3881/aa6572

Queloz, D., Eggenberger, A., Mayor, M., et al. 2000, A&A, 359, L13

Ricker, G. R., Winn, J. N., Vanderspek, R., et al. 2015, Journal of Astronomical Telescopes, Instruments, and Systems, 1, 014003, doi: 10.1117/1.JATIS.1.1.014003

Rossiter, R. A. 1924, ApJ, 60, doi: 10.1086/142825

Saad-Olivera, X., Nesvorný, D., Kipping, D. M., & Roig, F. 2017, AJ, 153, 198, doi: 10.3847/1538-3881/aa64e0

Sicardy, B., Ortiz, J. L., Assafin, M., et al. 2011a, Nature, 478, 493, doi: 10.1038/nature10550

Sicardy, B., Bolt, G., Broughton, J., et al. 2011b, AJ, 141, 67, doi: 10.1088/0004-6256/141/2/67

Southworth, J. 2010, MNRAS, 408, 1689, doi: 10.1111/j.1365-2966.2010.17231.x

Soutter, J., Horner, J., & Pepper, J. 2016, ArXiv e-prints. https://arxiv.org/abs/1605.02425

Swift, J. J., Bottom, M., Johnson, J. A., et al. 2015, Journal of Astronomical Telescopes, Instruments, and Systems, 1, 027002, doi: 10.1117/1.JATIS.1.2.027002

Tinney, C. G., Wittenmyer, R. A., Butler, R. P., et al. 2011, ApJ, 732, 31, doi: 10.1088/0004-637X/732/1/31

Turner, J. D., Leiter, R. M., Biddle, L. I., et al. 2017, MNRAS, 472, 3871, doi: 10.1093/mnras/stx2221

van de Kamp, P. 1963, AJ, 68, 515, doi: 10.1086/109001

Wang, S., Addison, B., Fischer, D. A., et al. 2018a, AJ, 155, 70, doi: 10.3847/1538-3881/aaa2fb

Wang, S., Wang, X.-Y., Wang, Y.-H., et al. 2018b, AJ, 156, 181, doi: 10.3847/1538-3881/aadcfc

Welsh, W. F., Orosz, J. A., Short, D. R., et al. 2015, ApJ, 809, 26, doi: 10.1088/0004-637X/809/1/26

Winn, J. N., & Fabrycky, D. C. 2015, ARA&A, 53, 409, doi: 10.1146/annurev-astro-082214-122246

Wittenmyer, R. A., Horner, J., Tinney, C. G., et al. 2014, ApJ, 783, 103, doi: 10.1088/0004-637X/783/2/103

Wittenmyer, R. A., Jones, M. I., Horner, J., et al. 2017, AJ, 154, 274, doi: 10.3847/1538-3881/aa9894

Wu, Y., & Lithwick, Y. 2011, ApJ, 735, 109, doi: 10.1088/0004-637X/735/2/109

Ziegler, C., Law, N. M., Baranec, C., et al. 2018, ArXiv e-prints. https://arxiv.org/abs/1806.10142